Theory of quantum-coherence phenomena in semiconductor quantum dots

W. W. Chow
Semiconductor Material and Device Sciences Department, Sandia National Laboratories, Albuquerque, New Mexico 87185-0601, USA

H. C. Schneider
Physics Department, Kaiserslautern University, P.O. Box 3049, 67653 Kaiserslautern, Germany

M. C. Phillips
Lasers, Optics and Remote Sensing Department, Sandia National Laboratories, Albuquerque, New Mexico 87185-1423, USA
(Received 21 May 2003; published 3 November 2003)

This paper explores quantum-coherence phenomena in a semiconductor quantum-dot structure. The calculations predict the occurrence of inversionless gain, electromagnetically induced transparency, and refractive-index enhancement in the transient regime for dephasing rates typical under room temperature and high excitation conditions. They also indicate deviations from atomic systems because of strong many-body effects. Specifically, Coulomb interaction involving states of the quantum dots and the continuum belonging to the surrounding quantum well leads to collision-induced population redistribution and many-body energy and field renormalizations that modify the magnitude, spectral shape, and time dependence of quantum-coherence effects.

DOI: 10.1103/PhysRevA.68.053802 PACS number(s): 42.50.Gy, 42.65.−k, 78.67.Hc

I. INTRODUCTION

During the last decade, advances in quantum optics led to experimental demonstrations of quantum-coherence phenomena, such as lasing without inversion (LWI), electromagnetically induced transparency (EIT), ultralarge refractive-index enhancement, and slow light [1]. These developments brought worldwide attention because quantum-mechanical coherence and interference are realized in a macroscopic system. Additionally, one can envision the development of a new generation of highly efficient, coherent and incoherent optical sources and detectors whose noise properties and sensitivities go beyond the standard quantum limits.

To date, EIT, LWI and other pump-probe schemes exploiting coherent polarizations have been investigated using different approaches in a large number of physical settings. Many of these results are classics of the quantum-optics literature and are discussed in recent review articles [2,3], where relevant references are also given. While most quantum-coherence experiments involve dilute systems (as in atomic or molecular vapors and doped solids) [4–7], there is also interest in realizing similar effects in semiconductors. A motivation is the potentially drastic increase in applications because of the widespread use of semiconductor components in optoelectronics. Quantum-coherence phenomena involving intersubband transitions in semiconductor quantum wells were investigated theoretically [8] and experimentally [9]. Recently, EIT was experimentally demonstrated using exciton and biexciton transitions in a quantum-well structure [10,11]. There are additional theoretical studies on LWI and refractive-index enhancement in semiconductor nanostructures for the purposes of coherent mid- to far-infrared radiation generation [12] and optical storage [13], respectively. There, steady-state results are obtained by assuming that a semiconductor system behaves analogous to an inhomogeneously broadened atomic system with strong dephasing effects.

This paper explores in more generality the extension of quantum-coherence phenomena to semiconductors. By examining the transient regime and employing a physically more realistic description of a semiconductor structure, we find interesting differences in the physics underlying semiconductor and atomic quantum-coherence phenomena. As alluded to earlier, dephasing processes are significantly faster because of carrier-carrier and carrier-phonon scattering. To overcome the greater loss of coherence, higher optical drive fields (i.e., higher Rabi frequencies) are necessary. The time scale for system dynamics will be in the tens of femtoseconds to picoseconds [14,15], instead of microseconds as in an atomic system. Moreover, one can no longer assume to have an isolated three-level system. A semiconductor quantum-coherence experiment will still involve a three-level system, e.g., consisting of excitonic or quantum-dot bound states. However, this three-level system will be energetically in close proximity to other quantum-dot bound states and to a continuum comprising states from the quantum well embedding the quantum dots. The Coulomb interaction couples discrete and continuum states, resulting in collision-induced carrier-population redistribution, as well as many-body energy and field renormalizations [16].

Section II presents the equations necessary for investigating quantum-coherence phenomena in semiconductors. The derivation of these equations is described in the Appendix. A semiclassical approach is used, which is based on the semiconductor Bloch equations [17] with many-body Coulomb effects treated at the level of the screened Hartree-Fock approximation. For this paper, a quantum-dot structure is considered because we believe that the transition from atomic and molecular systems to semiconductors is best accomplished with quantum dots. The three-dimensional quantum confinement gives an electronic structure that closely re-

sembles that of an atom, and may mitigate dephasing effects by providing some degree of isolation between quantum dots and the surrounding region. For realistic predictions of optical response, the theory requires as input details of the electronic structure, in particular, the bound-state energies, the energy dispersions of the continuum, and the oscillator strengths of the relevant transitions. Section III describes how these properties are determined from a band-structure calculation. The example of an $In_xGa_{1-x}N/Al_yGa_{1-y}N$ quantum-dot structure is chosen because it provides an opportunity to illustrate how quantum coherence can generate short-wavelength (ultraviolet) coherent radiation in a semiconductor system. To achieve this with conventional stimulated emission would require one to replace indium with aluminum in the active region, which at present inevitably increases defect density [18].

Section IV applies the tools developed in the previous two sections to study the nature of quantum coherence phenomena in a quantum-dot system. We show that when driven by a short, intense optical pulse, a quantum-dot structure can exhibit inversionless gain and EIT, as the system evolves with time. We refer to EIT as the reduction in absorption of the probe field under the action of a coherent drive field. Inversionless gain is said to occur if the drive field leads to gain in the probe transition without a population inversion in the drive or the probe transition. Considerable work has been performed to distinguish inversionless gain from coherent population trapping [19,20] or Raman gain [21] under cw (continuous wave) and pulsed conditions. The dephasing time was assumed to be short in the former, and considerably longer than the pulse duration in the latter. In this paper, our focus is on the transient pumping regime, where pulse lengths are comparable to the dephasing time. We will show that the interplay between quantum coherence and many-body effects leads to transient behaviors that are different from those found in atomic systems [22,23]. In particular, modifications to the inversionless gain and EIT dependence on probe frequency by the coupling to other quantum-dot bound states and to the continuum will be discussed. Also described is the refractive-index enhancement and the associated group-velocity reduction. Finally, we discuss the role of dephasing. To describe scattering effects at the level of a quantum kinetic theory [24] is beyond the scope of this study. Instead, we use an effective relaxation rate approximation and perform the calculations for the range of relaxation rates reported in the literature.

II. THEORY

Figure 1 depicts a typical energy-level diagram of a quantum-dot structure. There are quantum-dot electron and hole bound states, as well as the continuum states of the quantum well that embeds the quantum dots. With a quantum-coherence experiment in mind, and governed by dipole matrix selection rules, one picks three states from the many quantum-dot levels. Following the notation used for atomic systems, we denote these states as $|a\rangle$, $|b\rangle$, and $|c\rangle$. While optical transition matrix elements involving the electron state $|a\rangle$ and other hole states are typically small because of envelope function overlap arguments, these states (represented by dashed lines and shaded regions) still have to be included in the analysis because they play a role in the carrier-population redistribution by collisions. As will be shown later, these states additionally modify optical properties via many-body Coulomb effects.

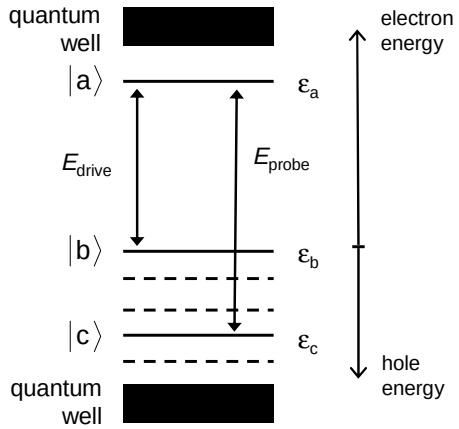

FIG. 1. Energy levels for quantum-dot structure. A band gap separates the electron ($|a\rangle$) and hole ($|b\rangle$) states. The solid lines indicate the levels directly involved in the quantum-coherence process, while the dashed lines and the shaded regions represent the other quantum-dot states and quantum-well continuum states that modify quantum-coherence behavior. The drive and probe fields are also shown.

The experimental setup calls for two optical fields: a drive field to pump the transition involving states $|a\rangle$ and $|b\rangle$, and a probe field for measuring the optical response at the transition involving states $|a\rangle$ and $|c\rangle$, as well as quantum-well electron and hole states $|e\mathbf{k}\rangle$ and $|h\mathbf{k}\rangle$, respectively. Working within the context of semiclassical laser theory, we write the total electric field as

$$E(z,t)=\frac{1}{2}[E_d(t)e^{ik_dz-i\omega_dt}+E_p(t)e^{ik_pz-i\omega_pt} + E_d(t)e^{-ik_dz+i\omega_dt}+E_p^*(t)e^{-ik_pz+i\omega_pt}], \quad (1)$$

where z is the position along the propagation direction, k_j is the wave vector, ω_j is the frequency, the subscripts d and p identify the drive and probe fields, and the slowly varying probe field amplitude E_p is complex to allow for a phase difference between it and the drive field (real) amplitude E_d. Derivation of the medium equations of motion is carried out in the Heisenberg picture using a Hamiltonian that contains the noninteracting plasma (free-carrier) energy, dipole-interaction energy with the optical fields, and Coulomb interaction energy among carriers (see the Appendix). Written explicitly for the polarizations connecting states $|a\rangle$, $|b\rangle$, and $|c\rangle$, Eqs. (A7) and (A8) in the Appendix become

$$\frac{dp_{ab}}{dt}=-(i\omega_{ab}+\gamma^d)p_{ab}-i\Omega_{ab}(n_a+n_b-1)+i\Omega_{ac}p_{cb}, \quad (2)$$

$$\frac{dp_{ac}}{dt} = -(i\omega_{ac}+\gamma^d)p_{ac} - i\Omega_{ac}(n_a+n_c-1) + i\Omega_{ab}p_{bc}, \tag{3}$$

$$\frac{dp_{bc}}{dt} = -(i\omega_{bc}+\gamma^d)p_{bc} + i(\Omega_{ba}p_{ac} - p_{ba}\Omega_{ac}) + i\Delta^{nd}_{bc}(n_b-n_c), \tag{4}$$

where collision effects are approximated using an effective dephasing rate γ^{d}, i.e., $\partial p_{\alpha\beta}|_{\mathrm{col}} \approx -\gamma^{\mathrm{d}} p_{\alpha\beta}$, and the electron (hole) populations in the dot and continuum states are denoted by $n_{\alpha'}$ $(n_{\beta'})$ and $n_{e\mathbf{k}'}$ $(n_{h\mathbf{k}'})$, respectively. Both the transition frequency $\omega_{\alpha\beta}$ and the Rabi frequency $\Omega_{\alpha\beta}$ are modified by many-body effects:

$$\omega_{\alpha\beta} = \omega^{(0)}_{\alpha\beta} + \Delta^d_{\alpha\beta}, \tag{5}$$

$$\Omega_{\alpha\beta} = \frac{\mu_{\alpha\beta}}{\hbar}E^+ + \Delta^{nd}_{\alpha\beta}, \tag{6}$$

where $\omega^{(0)}_{\alpha\beta}$ is the unexcited-material transition frequency, $\mu_{\alpha\beta}$ is the dipole matrix element, E^+ is the positive frequency part of Eq. (1) with $z=0$, and the many-body contributions are grouped into diagonal and nondiagonal terms $\Delta^d_{\alpha\beta}$ and $\Delta^{nd}_{\alpha\beta}$, respectively. Rewriting Eqs. (A14)–(A17) explicitly in terms of dot-dot and dot-well terms gives

$$\hbar\Delta^d_{\alpha\beta} = -\sum_{\alpha'} W^{\alpha\alpha}_{\alpha'\alpha'}n_{\alpha'} - \sum_{\beta'} W^{\beta\beta}_{\beta'\beta'}n_{\beta'} + \sum_{\beta'} (W^{\beta\beta}_{\beta'\beta'} - V^{\beta\beta}_{\beta'\beta'}) - \sum_{\mathbf{k}'} W^{\alpha\alpha}_{\mathbf{k}'\mathbf{k}'}n_{e\mathbf{k}'} - \sum_{\mathbf{k}'} W^{\beta\beta}_{\mathbf{k}'\mathbf{k}'}n_{h\mathbf{k}'} + \sum_{\mathbf{k}'} (W^{\beta\beta}_{\mathbf{k}'\mathbf{k}'} - V^{\beta\beta}_{\mathbf{k}'\mathbf{k}'}), \tag{7}$$

$$\hbar\Delta^{nd}_{\alpha\beta} = \sum_{\alpha',\beta'} W^{\alpha\beta}_{\alpha'\beta'}p_{\alpha'\beta'} + \sum_{\mathbf{k}} W^{\alpha\beta}_{\mathbf{k}\mathbf{k}}p_{\mathbf{k}}, \tag{8}$$

where the matrix elements for the screened and bare Coulomb interaction energy W and V are described by Eqs. (A20) and (A22), and the discussion following these equations. We neglected terms associated with space-charge effects (Hartree terms) and polarizations between continuum hole states. Implicit in the summations is no electron to hole or light-hole to heavy-hole coupling via the Coulomb interaction. Furthermore, because of the likelihood of $\gamma_d \gtrsim \omega_{\alpha\beta}$ in a semiconductor, we deviate from the atomic derivation and include terms typically neglected in the rotating-wave approximation.

Similarly, Eqs. (A9)–(A11) for the quantum-dot carrier population become

$$\frac{dn_a}{dt} = i(\Omega_{ab}p_{ba} - p_{ab}\Omega_{ba}) + i(\Omega_{ac}p_{ca} - p_{ac}\Omega_{ca}) - \gamma^d_{nr}n_a - \gamma^d_{c-c}[n_a - f_a(\mu^p_e, T_p)] - \gamma^d_{c-p}[n_a - f_a(\mu^l_e, T_l)], \tag{9}$$

$$\frac{dn_b}{dt} = i(\Omega_{ab}p_{ba} - p_{ab}\Omega_{ba}) - \gamma^d_{nr}n_b - \gamma^d_{c-c}[n_b - f_b(\mu^p_h, T_p)] - \gamma^d_{c-p}[n_b - f_b(\mu^l_h, T_l)], \tag{10}$$

$$\frac{dn_c}{dt} = +i(\Omega_{ac}p_{ca} - p_{ac}\Omega_{ca}) - \gamma^d_{nr}n_c - \gamma^d_{c-c}[n_c - f_c(\mu^p_h, T_p)] - \gamma^d_{c-p}[n_c - f_c(\mu^l_h, T_l)], \tag{11}$$

where γ^d_{nr}, γ^d_{c-c}, and γ^d_{c-p} are effective nonradiative recombination, carrier-carrier scattering, and carrier-phonon scattering rates, respectively. The population relaxation terms (second line in each equation) approximate the collision-induced particle exchange processes that tend to drive the population distributions n_β to quasiequilibrium Fermi-Dirac functions f_β at chemical potentials and temperatures (μ^p_α, T_p) and (μ^l_α, T_l), where T_p and T_l are the plasma and lattice temperatures, respectively.

As discussed at the beginning of this section, the states of the quantum well that embeds the quantum dots can influence quantum-dot optical behavior. The equations of motion for the quantum-well polarizations and populations (A12) and (A13) may be rewritten as

$$\frac{dp_{\mathbf{k}}}{dt} = -(i\omega_{\mathbf{k}}+\gamma^q)p_{\mathbf{k}} - i\Omega_{\mathbf{k}}[n_{e,\mathbf{k}} + n_{h,\mathbf{k}} - 1], \tag{12}$$

$$\frac{dn_{e,\mathbf{k}}}{dt} = i[\Omega_{\mathbf{k}}p^*_{\mathbf{k}} - p_{\mathbf{k}}\Omega^*_{\mathbf{k}}] - \gamma^q_{nr}n_{e,\mathbf{k}} - \gamma^q_{c-c}[n_{e,\mathbf{k}} - f_{e,\mathbf{k}}(\mu^p_e, T_p)] - \gamma^q_{c-p}[n_{e,\mathbf{k}} - f_{e,\mathbf{k}}(\mu^l_e, T_l)], \tag{13}$$

$$\frac{dn_{h,\mathbf{k}}}{dt} = i[\Omega_{\mathbf{k}}p^*_{\mathbf{k}} - p_{\mathbf{k}}\Omega^*_{\mathbf{k}}] - \gamma^q_{nr}n_{h,\mathbf{k}} - \gamma^q_{c-c}[n_{h,\mathbf{k}} - f_{h,\mathbf{k}}(\mu^p_h, T_p)] - \gamma^q_{c-p}[n_{h,\mathbf{k}} - f_{h,\mathbf{k}}(\mu^l_h, T_l)], \tag{14}$$

where $\mathbf{k}$ is the carrier momentum, and the other variables are the quantum-well equivalent of those for the quantum dots. Equations (2)–(4) and (9)–(11) are coupled to Eqs. (12)–(14) by the chemical potentials and plasma temperature. To determine the chemical potentials μ^p_e and μ^p_h, we note that total electron and hole densities are conserved in carrier-carrier collisions. Hence,

$$N_d\sum_\alpha n_\alpha + \frac{1}{A}\sum_{\mathbf{k}} n_{e,\mathbf{k}} = N_d\sum_\alpha f_\alpha(\mu^p_e, T_p) + \frac{1}{A}\sum_{\mathbf{k}} f_{e,\mathbf{k}}(\mu^p_e, T_p), \tag{15}$$

$$N_d\sum_\beta n_\beta+\frac{1}{A}\sum_{\mathbf{k}} n_{h,\mathbf{k}} = N_d\sum_\beta f_\beta(\mu_h^p,T_p)+\frac{1}{A}\sum_{\mathbf{k}} f_{h,\mathbf{k}}(\mu_h^p,T_p), \tag{16}$$

where N_d is the density of quantum dots, A is the active region area, and the summations over α and β involve all electron and hole quantum-dot states, respectively. Also conserved in carrier-carrier collisions is the total electron and hole energy, which specifies the plasma temperature T_p via

$$N_d\left(\sum_\alpha \varepsilon_\alpha n_\alpha+\sum_\beta \varepsilon_\beta n_\beta\right)+\frac{1}{A}\sum_{\sigma=e,h}\sum_{\mathbf{k}} \varepsilon_{\sigma,\mathbf{k}} n_{\sigma,\mathbf{k}} = N_d\left[\sum_\alpha \varepsilon_\alpha f_\alpha(\mu_e^p,T_p)+\sum_\beta \varepsilon_\beta f_\beta(\mu_h^p,T_p)\right] + \frac{1}{A}\sum_{\sigma=e,h}\sum_{\mathbf{k}} \varepsilon_{\sigma,\mathbf{k}} f_{\sigma,\mathbf{k}}(\mu_\sigma^p,T_p), \tag{17}$$

where ε_α ($\varepsilon_{e,\mathbf{k}}$) and ε_β ($\varepsilon_{h,\mathbf{k}}$) are the quantum-dot (quantum-well) energies for electrons and holes, respectively. For the quasiequilibrium distributions $f_i(\mu_\sigma^l,T_l)$ and $f_{\sigma,\mathbf{k}}(\mu_\sigma^l,T_l)$ reached by carrier-phonon collisions, the total carrier density is again conserved, which gives

$$N_d\sum_\alpha n_\alpha+\frac{1}{A}\sum_{\mathbf{k}} n_{e,\mathbf{k}} = N_d\sum_\alpha f_\alpha(\mu_e^l,T_l)+\frac{1}{A}\sum_{\mathbf{k}} f_{e,\mathbf{k}}(\mu_e^l,T_l),$$

$$N_d\sum_\beta n_\beta+\frac{1}{A}\sum_{\mathbf{k}} n_{h,\mathbf{k}} = N_d\sum_\beta f_\beta(\mu_h^l,T_l)+\frac{1}{A}\sum_{\mathbf{k}} f_{h,\mathbf{k}}(\mu_h^l,T_l). \tag{18}$$

However, energy is exchanged between carriers and lattice, which we take into account by fixing the temperature of the quasiequilibrium distributions in Eq. (18) to the lattice temperature T_l. An attraction of the above approach is that the transport of carriers between the quantum-dot and quantum-well subsystems is described as an integral part of the relaxation processes due to collisions.

III. BAND STRUCTURE

In Eqs. (5) and (6), the transition energies $\omega_{ij}^{(0)}$ and dipole transition matrix elements μ_{ij} are properties of the electronic structure. As discussed in the Introduction, we consider a quantum-dot structure consisting of $In_{0.10}Ga_{0.90}N$ quantum dots embedded in a 2-nm-thick $Al_{0.15}Ga_{0.85}N$ quantum well, which is cladded by $Al_{0.20}Ga_{0.80}N$ layers. The shape of an $In_{0.1}Ga_{0.9}N$ quantum dot is approximated by a 2-nm-high truncated cone, with top and bottom diameters of 4 nm and 8 nm, respectively. When calculating the electronic structure, we assume that the quantum confinement and built-in electrostatic potential is appreciably weaker in the radial direction than in the vertical direction, so that it is possible to make a separation of variables in the vertical and lateral dimensions [25]. With this simplification, the quantum-dot states are obtained by simultaneously solving Schrödinger and Poisson equations in each dimension. The solutions contain the effects of the quantum confinement, the built-in electric field, and the mixing between hole states. For computing the quantum-well states, we use a multiband $\mathbf{k}\cdot\mathbf{p}$ model in the envelope approximation [26]. The input to the electronic structure calculations are the bulk material properties such as the electron and hole effective masses, crystal-field and spin-orbit energy splittings, elastic constants, lattice constants, and deformation potentials [27]. The remaining parameters are the bulk material dipole matrix element ($e\times 2.3$ nm), background refractive index (2.28), permittivity of the host material ($10.6\varepsilon_0$), and band-offset energies (60:40 conduction:valence band-offset ratio assumed).

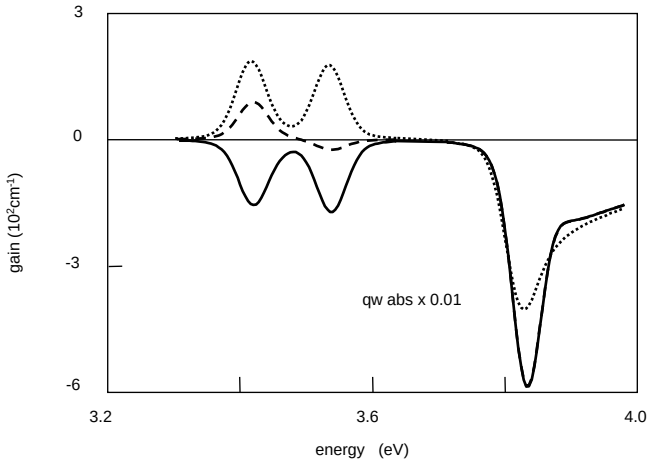

FIG. 2. Room-temperature absorption and gain spectra in the absence of a drive field, showing the optical transitions of $In_{0.1}Ga_{0.9}N$ quantum-dot structure used in the present study. The carrier densities are $N=10^{10}$ (solid curve), 10^{11} (dashed curve), and 10^{12} cm^{-2} (dotted curve). The energetically lower (higher) peak belongs to the electron to heavy-hole (light-hole) transition, which corresponds to the $a\rightarrow b$ ($a\rightarrow c$) transition in Fig. 1.

To illustrate the electronic structure contributions to optical properties, we show in Fig. 2 the calculated linear absorption and gain spectra for different carrier densities. The absorption or gain is a part of the complex susceptibility χ that is related to the electron-hole polarization according to

$$k_d\delta n-ig=n_b k_d\chi=\frac{\omega_d}{\varepsilon_0 n_b c|E_p|w}\times\left(N_d\sum_\alpha\sum_\beta \mu_{a\beta}p_{a\beta}+\frac{1}{A}\sum_{\mathbf{k}} \mu_{\mathbf{k}}p_{\mathbf{k}}\right), \tag{19}$$

where g is the linear (small signal) amplitude gain, δn is the carrier-induced refractive-index change, ε_0 and c are the permittivity and speed of light in vacuum, w is the thickness of the active region, and n_b is the background refractive index.

To obtain the spectra in Fig. 2, $p_{\alpha\beta}$ and $p_{\mathbf{k}}$ are computed in the absence of the drive field and, consequently, with no quantum-interference contributions. We assume a dot density of $N_d = 5\times10^{10}$ cm^{-2}, an inhomogeneous broadening of 20 meV, dephasing rates of $\gamma^d = \gamma^q = 10^{13}$ s^{-1}, and quasiequilibrium between quantum-dot and quantum-well populations. The two-dimensional carrier density is

$$N = 2N_d \sum_{\alpha} n_{\alpha} + \frac{2}{A} \sum_{\mathbf{k}} n_{\sigma_{\alpha}\mathbf{k}}, \tag{20}$$

where, assuming charge neutrality, the summation need only be over either electron or hole states.

Figure 2 shows that at low carrier density, the spectra exhibit the familiar signature of excitonic absorption. With increasing carrier density, the excitonic resonances are gradually bleached and, eventually, optical gain appears in the vicinities of the original exciton resonances. Contributing to the quantum-dot portion of each optical spectrum are transitions involving one electron and six hole quantum-dot states. Transitions involving the lowest-order lateral eigenmodes give rise to two pronounced resonances, where the lower- (higher-) energy resonance is a result of an electron to heavy- (light-) hole transition. Also present are the strong quantum-well exciton and interband absorption. The contributions from transitions involving higher-order lateral quantum numbers are not resolvable because their amplitudes are noticeably weaker as a result of dipole selection rules. The spectra indicate that a carrier density greater than 10^{11} cm^{-2} is necessary for the appearance of gain in the electron to light-hole, i.e., high-energy, transition. In the following section, we will explore the feasibility of achieving gain at this transition with a lower carrier density via quantum coherence.

IV. RESULTS

First, we consider the situation where we apply an optical drive pulse to the quantum-dot structure described in the preceding section. The pulse is assumed to be resonant with the electron to heavy-hole transition at frequency $\omega_{ab}^{(0)}$, and we examine the optical response close to the electron to light-hole transition frequency $\omega_{ac}^{(0)}$. The optical response is determined by the time-dependent polarizations $p_{\alpha\beta}(t)$ and $p_{\mathbf{k}}(t)$. We present the results in the form of a gain $g(t)$ and refractive index $\delta n(t)$ as given by Eq. (19), where the values of $p_{\alpha\beta}(t)$ and $p_{\mathbf{k}}(t)$ are averaged over the probe field phase.

Figures 3(a) and 3(b) show the temporal relationship between drive pulse and optical response to weak probe signal. In the calculation, we assume dephasing and collision rates $\gamma^d = \gamma_{c-c} = \gamma^q = \gamma^q_{c-c} = 2\times10^{12}$ s^{-1}, $\gamma_{c-p} = \gamma^q_{c-p} = 5\times10^{11}$ s^{-1}, $\gamma_{nr} = \gamma^q_{nr} = 10^9$ s^{-1}, and we use the units of cm^{-1} (inverse propagation length) for the optical response to facilitate comparison with gain and absorption produced by conventional excitation methods (as in Fig. 2). For a probe applied at slightly higher energy than $\omega_{ac}^{(0)}$, there is an abrupt bleaching of the absorption after the onset of the drive pulse. This is followed by the appearance of gain for a very short duration, after which absorption reappears, but at a smaller value than prior to the drive pulse. Figure 3(c) indicates that the *a*-*b* and *a*-*c* transitions are not inverted, even during the period when the probe signal experiences optical gain. It should be noted that, even though the individual transitions are not inverted, there exists a Raman gain $n_{\mathrm{hh}} - n_{\mathrm{lh}} = n_b - n_c > 0$ for the duration of the pulse, in accordance with a result of Ref. [21]. Carrier density (created by the drive pulse) at the gain maximum is $N \lesssim 5\times10^9$ cm^{-2}, which is over an order of magnitude lower than that necessary to reach transparency in the electron to light-hole transition in the absence of quantum interference (see dashed curve in Fig. 2). However, it should be noted that in this transient inversionless gain case, the carrier distribution created by the drive pulse has a significantly lower kinetic energy, as characterized by a plasma temperature of $T_p = 140$ K in an equivalent quasiequilibrium distribution.

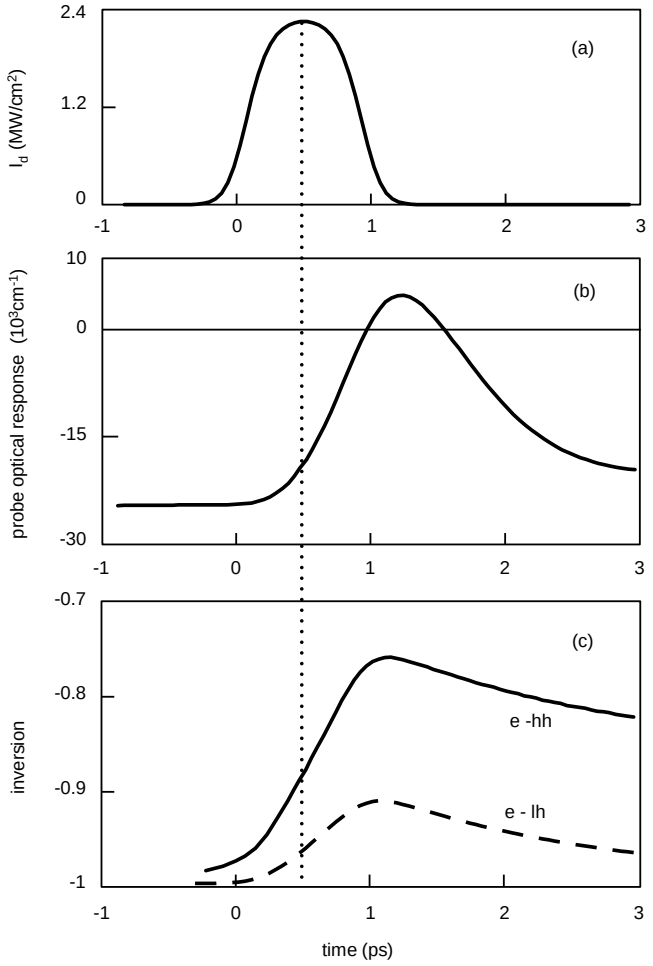

FIG. 3. (a) Drive pulse, (b) probe optical response, and (c) inversion in electron to heavy-hole (solid curve) and light-hole (dashed curve) transition vs time, which correspond, respectively, to the $a \rightarrow b$ and $a \rightarrow c$ transitions in Fig. 1.

Figure 4 describes, in greater detail, the nature of the optical response. Each curve shows the probe frequency dependence of the optical response at different times. At the start of the drive pulse, one has the typical excitonic absorption resonance centered at $\omega_{ac}^{(0)}$ (dotted curve). The dashed curve

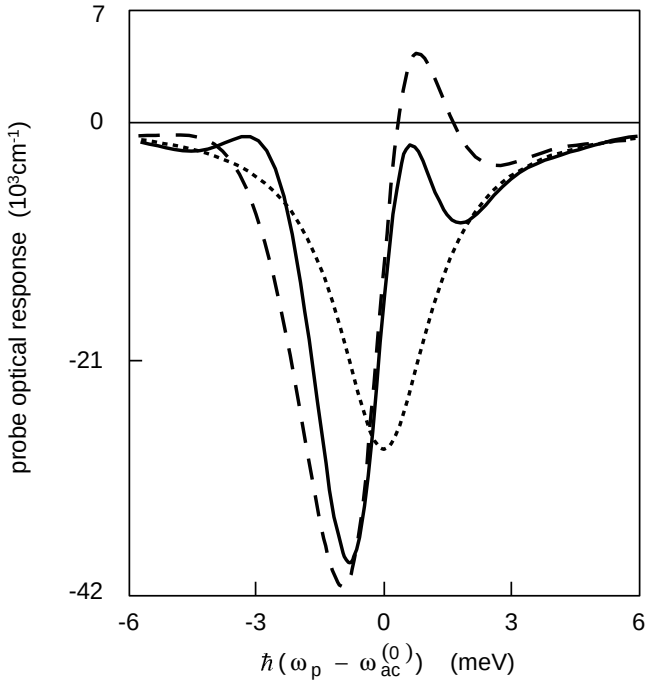

FIG. 4. Optical response vs probe frequency at (a) $t=0$ (dotted curve), (b) 1.2 ps (dashed curve), and (c) 1.6 ps (solid curve).

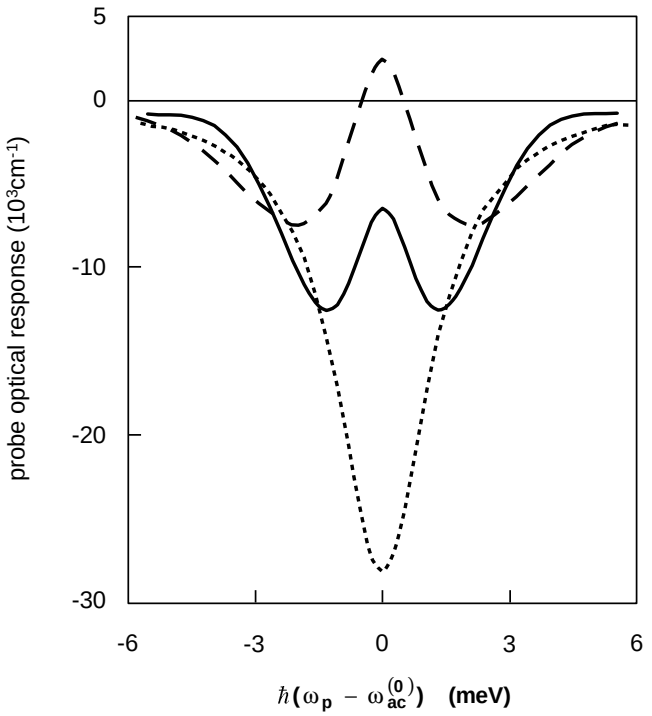

FIG. 5. Free-carrier optical response vs probe frequency during the start of drive pulse (dotted curve), peak of inversionless gain (dashed curve), and peak of EIT (solid curve).

shows the presence of inversionless gain shortly afterwards, which evolves into the solid curve indicating the presence of EIT. Both features are highly transient, and the optical response returns to the usual absorption spectrum at long times. The quantum-coherence effects occur concurrently with the bleaching of absorption due to carrier creation and population redistribution. In the transient regime, the plasma is appreciably cooler than the lattice ($T_p \ll T_l$) because the system dynamics is occurring on a time scale that is shorter than the carrier-phonon collision time.

Dephasing processes and the transient nature of the drive field determine to a large extent the system dynamics described in Figs. 3 and 4. When extended to the steady-state limit, our calculations show that the quantum coherence leading to EIT remains, although the transient inversionless gain disappears. To recover the inversionless gain, one can externally inject carriers into $|a\rangle$ and $|c\rangle$, while still maintaining an uninverted population between these states. External carrier injection can also be used to prolong the gain duration in the transient case.

The exact spectral and temporal response naturally depend on the details the drive and probe pulses. Additional calculations (not presented) indicate that spectral features similar to those shown in Fig. 4 are also present for probe pulse duration shorter than drive pulse duration, as may be the case in a transient pump-probe experiment. A parametric study of the dependence of the optical response on the shapes, durations, and magnitudes of the drive and probe pulses is not the intent of this paper. Instead, we will now concentrate on the differences to the optical response caused by semiconductor many-body effects.

The curves in Fig. 4 exhibit features that are unique to semiconductors. These features are a result of many-body effects, specifically, the Hartree-Fock renormalizations and population redistribution by carrier-carrier collisions. We compare the present results with those obtained by neglecting the Coulomb renormalizations $\Delta_{\alpha\beta}^{d}$ and $\Delta_{\alpha\beta}^{nd}$, and population relaxation to quasiequilibrium distributions (setting $\gamma_{c-c}=\gamma_{c-c}^{q}=\gamma_{c-p}=\gamma_{c-p}^{q}=0$). In doing so, we have essentially isolated $|a\rangle$, $|b\rangle$, and $|c\rangle$ from other quantum-dot and quantum-well states. Figure 5 shows the resulting optical response prior to the drive pulse arrival (dotted curve), and when inversionless gain and EIT are most prominent (dashed and solid curves, respectively). We see that in this free-carrier approximation, the signatures for the inversionless gain and EIT resemble those in the atomic case. Comparison with Fig. 4 shows that the many-body renormalizations give rise to highly asymmetrical spectra resulting from redistribution of optical response about $\omega_{ac}^{(0)}$. (Note that $\omega_{ac}^{(0)}$ are different because of the contribution from the exciton binding energy in Fig. 4.) To produce roughly the same degree of quantum-coherence effects in the two figures, a higher drive field amplitude is needed in Fig. 5, because of the absence of Coulomb enhancement and the incoherent pumping of the a-c transition by carrier-carrier collisions that transfer holes created by the drive pulse in $|b\rangle$ to $|c\rangle$.

Using Eq. (19) and the real part of the susceptibility, one obtains the carrier-induced refractive index spectra. Figure 6(a) shows δn as a function of probe frequency before the drive pulse (dotted curve), at the peak of inversionless gain (dashed curve), and when EIT is most prominent (solid curve). For comparison, Fig. 6(b) shows the results when Coulomb effects and collision-induced population transfer are neglected. The increase in structure caused by quantum

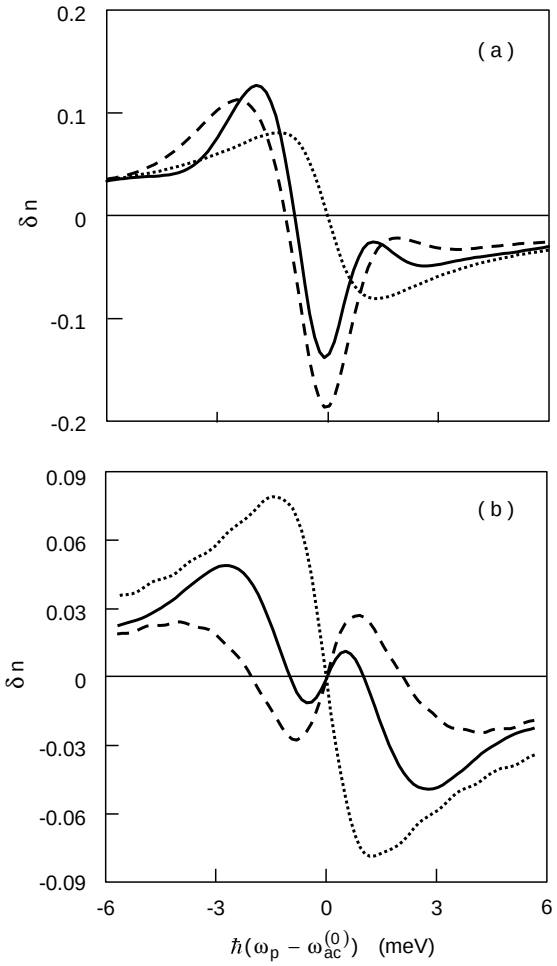

FIG. 6. Carrier-induced refractive-index change vs probe frequency (a) with and (b) without many-body renormalizations and population relaxation. The spectra are for the start of drive pulse (dotted curve), peak of inversionless gain (dashed curve), and peak of EIT (solid curve).

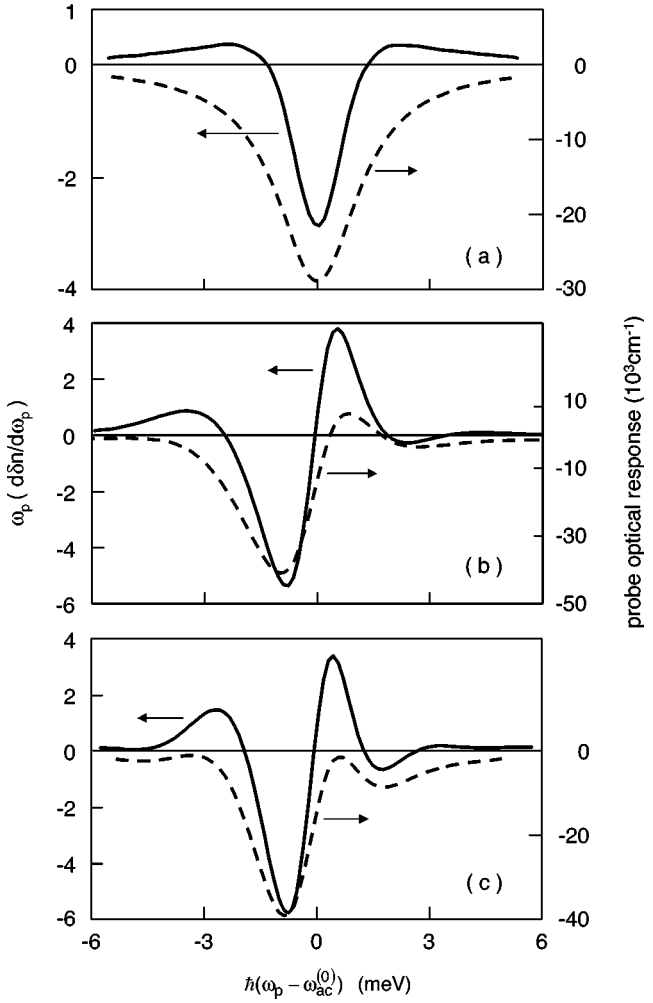

FIG. 7. Group-velocity reduction factor (solid curve) vs probe frequency during the (a) start of drive pulse, (b) peak of inversionless gain, and (c) peak of EIT. The dashed curves are the corresponding gain or absorption spectra.

coherence is clearly noticeable in both figures. However, the dot-dot and dot-well Coulomb interaction resulting in enhancement of the absorption are even more prominent in the refractive index. Both the shape and the magnitude of the changes in δn with detuning are distinctly different. Peak-to-valley changes in δn are three times greater in Fig. 6(a) than in Fig. 6(b). These index variations with detuning translate directly to modification in the group velocity $\mathbf{v}_g$ via the relationship

$$\mathbf{v}_g = \frac{c}{[n_b + \omega_p(d\,\delta n/d\,\omega_p)]}. \tag{21}$$

In Fig. 7, $\omega_p d\,\delta n/d\,\omega_p$ versus detuning for the three situations is plotted. Before the appearance of the drive pulse and at zero detuning, we see the expected increase in group velocity (i.e., $\omega_p d\,\delta n/d\,\omega_p < 0$) in an absorptive transition [Fig. 7(a)]. On the other hand, a reduction in group velocity ($\omega_p d\,\delta n/d\,\omega_p > 0$) is predicted in the presence of inversionless gain and EIT [Figs. 7(b) and 7(c)].

As in the atomic experiments, dephasing plays an important role in the semiconductor quantum-coherence effects. For a quantum-dot structure, there is much uncertainty in the carrier-carrier and carrier-phonon collision rates. Under high excitation (which is the case after the arrival of the drive pulse), the carrier-carrier scattering rate is typically an order of magnitude larger than the carrier-phonon scattering rate and, therefore, determines the dephasing rates γ^d and γ^q. Values for γ_{c-c} reported in the literature range from 10^{11} to 2×10^{14} s^{-1}, depending on experimental conditions. To obtain some indication of the sensitivity of quantum-coherence effects to the dephasing rate, we perform calculations for the collision rates $\gamma^d = \gamma^q = \gamma_{c-c} = 1\times10^{12}$, 2×10^{12}, and 3×10^{12} s^{-1}. Figure 8 summarizes the results for the gain or absorption and $\omega_p(d\,\delta n/d\,\omega_p)$. The same drive pulse as in Fig. 3(a) is used, and the plotted curves are for times when coherence effects are close to maximum for the three cases, i.e., when either the inversionless gain or EIT signature is most prominent. By comparing the solid and dashed curves in Fig. 8(a), one sees that the system goes from having inversionless gain to exhibiting only EIT when γ^d increases from 10^{12} s^{-1} to 2×10^{12} s^{-1}. For $\gamma^d = 3\times10^{12}$ s^{-1}, the only evidence of the presence of quantum coherence is the

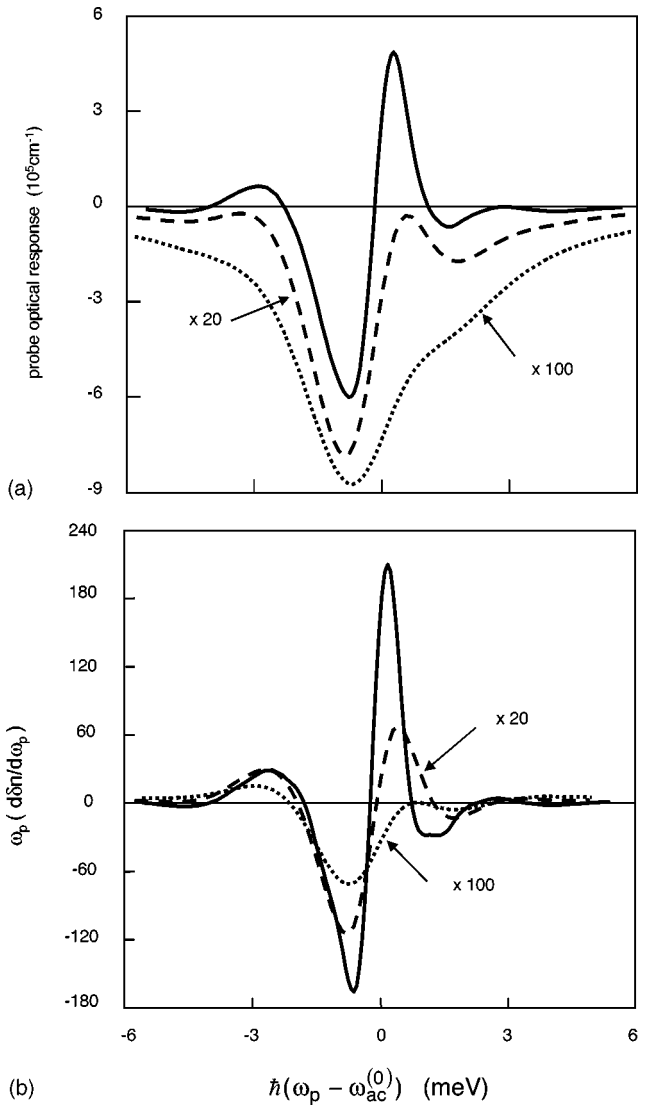

FIG. 8. (a) Probe gain or absorption and (b) group-velocity reduction factor spectra at $t=1.6$ ps for dephasing rates $\gamma^d = 1\times10^{12}$ (solid curve), 2×10^{12} (dashed curve) and 3×10^{12} s^{-1} (dotted curve).

slight flattening in the absorption spectrum (dotted curve). As discussed earlier, the asymmetry around zero detuning is caused by many-body renormalizations involving the quantum-dot and quantum-well population. In the dotted curve, this asymmetry is more visible than the spectral flattening, suggesting that many-body effects overtake quantum-coherence effects somewhere between $\gamma^d = 2\times10^{12}$ s^{-1} and $\gamma^d = 3\times10^{12}$ s^{-1}. Note the large multiplicative factors indicating the significant variation in spectral feature size for the small range of collision rates considered. The dotted curve in Fig. 8(b) clearly shows no group-velocity reduction for $\gamma^d = 3\times10^{12}$ s^{-1}. Even though $\omega_p(d\delta n/d\omega_p)$ remains negative, its zero detuning value is substantially greater than prior to the arrival of the drive pulse. As shown by the dashed curve, the results change significantly when the dephasing rate is reduced to $\gamma^d = 2\times10^{12}$ s^{-1}. Here, $\omega_p(d\delta n/d\omega_p) > 0$ at zero detuning, indicating the presence of group-velocity reduction. Further decreasing γ^d to 10^{12} s^{-1} gives a 60-fold increase in group-velocity reduction [i.e., $\omega_p(d\delta n/d\omega_p)$ increases from 3.5 at $\gamma^d = 2\times10^{12}$ s^{-1} to 220 at $\gamma^d = 10^{12}$ s^{-1}]. Finally, we note that accompanying the increase in group-velocity reduction is a sharpening of the spectral features, so that there is a tradeoff between maximizing quantum-coherence effects and tolerance to inhomogeneous broadening in the quantum-dot sample.

V. CONCLUSION

The implementation of recent advances in atomic quantum coherence and interference in a semiconductor system is explored theoretically using a microscopic theory of optical response. Our calculations predict the occurrence of inversionless gain, EIT, and refractive-index enhancement in the transient regime for a quantum-dot structure, even for dephasing rates typical under room temperature and high excitation conditions. They also indicate important deviations from atomic systems, because of strong influences from other quantum-dot states and from the continuum consisting of states from the surrounding quantum well. As a result, a quantum-dot structure should not be treated as an isolated few-level system. The dot-dot and dot-well Coulomb interaction gives rise to collision-induced population redistribution and many-body energy and field renormalizations. Together, they modify the magnitude, spectral shape, and time dependence of quantum-coherence effects.

ACKNOWLEDGMENTS

We thank M. Fleischhauer, S. W. Koch, and M. O. Scully for stimulating and fruitful discussions. W.W.C. acknowledges support from the Humboldt Foundation. This work was funded in part by the U.S. Department of Energy under Contract No. DE-AC04-94AL85000.

APPENDIX: DERIVATION OF THE EQUATIONS OF MOTION

For an interacting electron-hole plasma in a quantum-dot structure, the Hamiltonian is

$$H = H_0 + H_{c-f} + H_C, \tag{A1}$$

which contains contributions from the free-carrier energy,

$$H_0 = \sum_n \varepsilon_n a_n^\dagger a_n + \sum_m \varepsilon_m b_m^\dagger b_m, \tag{A2}$$

the carrier-laser-field interaction energy,

$$H_{c-f} = -\sum_{n,m} (\mu_{nm} a_n^\dagger b_m^\dagger + \mu_{nm}^* b_m a_n) E(z,t), \tag{A3}$$

and the Coulomb interaction energy,

$$H_C = \frac{1}{2}\sum_{n,m,r,s} W_{nm}^{rs} a_r^\dagger a_s^\dagger a_m a_n + \frac{1}{2}\sum_{n,m,r,s} W_{nm}^{rs} b_r^\dagger b_s^\dagger b_m b_n - \sum_{n,m,r,s} W_{nm}^{rs} a_r^\dagger b_s^\dagger b_m a_n. \tag{A4}$$

In the above equations, a_n and $a_n^\dagger$ are electron annihilation and creation operators, b_m and $b_m^\dagger$ are the corresponding operators for holes, ε_n is the free-carrier electron or hole energy, μ_{nm} is the dipole matrix element between states n and m, and the optical field is defined as in Eq. (1) in the main paper. The english alphabet subscripts and superscripts refer to either quantum-dot or quantum-well states. Later, when we distinguish between quantum-dot and quantum-well contributions, we will use greek alphabets to label quantum-dot states and the wave vector $\mathbf{k}$ to label quantum-well states. In instances where the carrier charge is not obvious, we use $\sigma_n = e$ or h to define the charge in state n. Equation (A4) contains the Coulomb interaction energy matrix element

$$\begin{aligned} W_{nm}^{rs} &= \int d^2r_1 \int d^2r_2 \phi_r^*(\mathbf{r}_1)\phi_n(\mathbf{r}_1) W(\mathbf{r}_1-\mathbf{r}_2) \\ &\quad \times \phi_s^*(\mathbf{r}_2)\phi_m(\mathbf{r}_2) \\ &= \sum_{\mathbf{q}\neq 0} W_q \int d^2r_1 \phi_r^*(\mathbf{r}_1) e^{-i\mathbf{q}\cdot\mathbf{r}_1}\phi_n(\mathbf{r}_1) \\ &\quad \times \int d^2r_2 \phi_s^*(\mathbf{r}_2) e^{-i\mathbf{q}\cdot\mathbf{r}_2}\phi_m(\mathbf{r}_2), \end{aligned} \tag{A5}$$

where $\phi_n(\mathbf{r})$ is the dot or well wave function in the quantum-well plane,

$$W_q = \frac{V_q}{\varepsilon_q} = \frac{1}{\varepsilon_q}\frac{e^2}{2A\varepsilon_b q} \tag{A6}$$

is the Fourier transform of the screened Coulomb potential, e is the electron charge, A is the area of the quantum well containing the quantum dots, ε_b is the host dielectric constant, and ε_q is the dimensionless longitudinal dielectric function calculated using the static Lindhard formula [24].

Using the above Hamiltonian, we proceed by working in the Heisenberg picture to derive the equations of motion for the polarizations , as well as the electron and hole populations. For brevity, we consider only the quantum-coherence scheme consisting of one quantum-dot electron state $|\alpha\rangle$ and two quantum-dot hole states $|\beta\rangle$ and $|\kappa\rangle$. After some simple but lengthy operator rearrangements, followed by the factorization of four-operator terms into products of the interband polarization $p_{\alpha\beta} = \langle b_\beta a_\alpha\rangle$, intraband polarization $p_{\beta\kappa} = \langle b_\kappa b_\beta^\dagger\rangle$, electron population $n_\alpha = \langle a_\alpha^\dagger a_\alpha\rangle$, and hole populations $n_\beta = \langle b_\beta^\dagger b_\beta\rangle$ and $n_\kappa = \langle b_\kappa^\dagger b_\kappa\rangle$, the results are obtained in the screened Hartree-Fock limit. For the polarizations, the equations of motion are

$$\begin{aligned} \frac{dp_{\alpha\beta}}{dt} &= -i\omega_{\alpha\beta}^{(0)} p_{\alpha\beta} - \frac{i}{2\hbar}[\mu_{\alpha\beta}(n_\alpha + n_\beta - 1) - \mu_{\alpha\kappa}p_{\kappa\beta}]E^+ \\ &\quad - i\Delta_{\alpha\beta}^d p_{\alpha\beta} - i\Delta_{\alpha\beta}^{nd}(n_\alpha + n_\beta - 1) + i\Delta_{\alpha\kappa}^{nd} p_{\kappa\beta} \\ &\quad + \left.\frac{\partial p_{\alpha\beta}}{\partial t}\right|_{col}. \end{aligned} \tag{A7}$$

and

$$\begin{aligned} \frac{dp_{\beta\kappa}}{dt} &= -i\omega_{\beta\kappa}^{(0)} p_{\beta\kappa} - \frac{i}{2\hbar}[\mu_{\alpha\kappa}p_{\beta\alpha}E^+ - \mu_{\beta\alpha}p_{\alpha\kappa}E^-] \\ &\quad - i\Delta_{\beta\kappa}^d p_{\beta\kappa} + i\Delta_{\beta\kappa}^{nd}(n_\beta - n_\kappa) + i[\Delta_{\beta\alpha}^{nd}p_{\alpha\kappa} - \Delta_{\alpha\kappa}^{nd}p_{\beta\alpha}] \\ &\quad + \left.\frac{\partial p_{\beta\kappa}}{\partial t}\right|_{col}, \end{aligned} \tag{A8}$$

where $E^{+/-}$ is the positive/negative frequency part of the optical field $E(0,t)$, $\hbar\omega_{\alpha\beta}^{(0)} = \varepsilon_\alpha + \varepsilon_\beta$, and $\hbar\omega_{\beta\kappa}^{(0)} = \varepsilon_\kappa - \varepsilon_\beta$. The last term in each of the above and the following equations with $\partial/\partial t|_{col}$ represents the collision contributions, and the actual form used in our calculation is discussed in the main paper. In addition, there are equations of motion for the carrier population in the single-electron level:

$$\begin{aligned} \frac{dn_\alpha}{dt} &= -\mathrm{Im}\left[\frac{1}{\hbar}(\mu_{\alpha\beta}p_{\beta\alpha} + \mu_{\alpha\kappa}p_{\kappa\alpha})E^+ + 2(\Delta_{\alpha\beta}^{nd}p_{\beta\alpha} \right. \\ &\quad \left. + \Delta_{\alpha\kappa}^{nd}p_{\kappa\alpha})\right] + \left.\frac{\partial n_a}{\partial t}\right|_{col} \end{aligned} \tag{A9}$$

and the double hole levels:

$$\frac{dn_\beta}{dt} = -\mathrm{Im}\left(\frac{1}{\hbar}\mu_{\alpha\beta}p_{\beta\alpha}E^+ + 2\Delta_{\alpha\beta}^{nd}p_{\beta\alpha}\right) + \left.\frac{\partial n_\beta}{\partial t}\right|_{col}, \tag{A10}$$

$$\frac{dn_\kappa}{dt} = -\mathrm{Im}\left(\frac{1}{\hbar}\mu_{\alpha\kappa}p_{\kappa\alpha}E^+ + 2\Delta_{\alpha\kappa}^{nd}p_{\kappa\alpha}\right) + \left.\frac{\partial n_\kappa}{\partial t}\right|_{col}. \tag{A11}$$

The derivation also gives the equations of motion for the quantum-well operators, i.e.,

$$\begin{aligned} \frac{dp_{\mathbf{k}}}{dt} &= -i\omega_{\mathbf{k}}p_{\mathbf{k}} - \frac{i}{2\hbar}\mu_{\mathbf{k}}E^+(n_{e\mathbf{k}} + n_{h\mathbf{k}} - 1) - i\Delta_{\mathbf{k}}^d p_{\mathbf{k}} \\ &\quad - i\Delta_{\mathbf{k}}^{nd}(n_{e\mathbf{k}} + n_{h\mathbf{k}} - 1) + \left.\frac{\partial p_{\mathbf{k}}}{\partial t}\right|_{col}, \end{aligned} \tag{A12}$$

$$\frac{dn_{\sigma\mathbf{k}}}{dt} = -\mathrm{Im}\left(\frac{1}{\hbar}\mu_{\mathbf{k}}p_{\mathbf{k}}^*E^+ + 2\Delta_{\mathbf{k}}^{nd}p_{\mathbf{k}}^*\right) + \left.\frac{\partial n_{\sigma\mathbf{k}}}{\partial t}\right|_{col}. \tag{A13}$$

Equations (A7)–(A13) contain contributions from many-body effects. In Eqs. (A7) and (A8) we have diagonal (superscript d) Coulomb terms that renormalize the transition frequencies. For interband transitions, the renormalization energy is

$$\begin{aligned} \hbar\Delta_{\alpha\beta}^d &= -\sum_n (W_{nn}^{\alpha\alpha} - W_{\alpha n}^{\alpha n})n_n - \sum_m (W_{mm}^{\beta\beta} - W_{\beta m}^{\beta m})n_m \\ &\quad + \sum_m (W_{mm}^{\beta\beta} - V_{mm}^{\beta\beta}) + \sum_m (W_{\beta m}^{\beta m} - V_{\beta m}^{\beta m}), \end{aligned} \tag{A14}$$

where α, n (β,m) denote the electron (hole) states and the summations are over both quantum-dot and quantum-well states. For intraband transitions,

$$\Delta^d_{\beta\kappa} = \Delta^d_{\alpha\kappa} - \Delta^d_{\alpha\beta}. \tag{A15}$$

Also present in Eqs. (A7)–(A10) are nondiagonal (superscript nd) Coulomb terms describing the Rabi frequency renormalization,

$$\hbar\Delta^{nd}_{\alpha\beta} = \sum_n \sum_m W^{\alpha\beta}_{nm} p_{nm}, \tag{A16}$$

$$\hbar\Delta^{nd}_{\beta\kappa} = \sum_m \sum_{m'} W^{\beta\kappa}_{mm'} p_{mm'}. \tag{A17}$$

Similarly, for the quantum-well equations,

$$\hbar\Delta^d_{\mathbf{k}} = -\sum_{\mathbf{k}'\neq\mathbf{k}} W_{|\mathbf{k}-\mathbf{k}'|}(n_{e\mathbf{k}'} + n_{h\mathbf{k}'}) \tag{A18}$$

and

$$\hbar\Delta^{nd}_{\mathbf{k}} = \sum_{\mathbf{k}'\neq\mathbf{k}} W_{|\mathbf{k}-\mathbf{k}'|} p_{\mathbf{k}'}, \tag{A19}$$

where $W_{|\mathbf{k}-\mathbf{k}'|}$ is as defined in Eq. (A6).

Finally, the Coulomb interaction energy matrix elements involving only quantum-dot states have the form

$$W^{\alpha\beta}_{\alpha'\beta'} = \sum_{\mathbf{q}\neq 0} W_q I_{\alpha\alpha'}(\mathbf{q}) I_{\beta'\beta}(\mathbf{q}), \tag{A20}$$

where α and β may be electron or hole states and the overlap integral is

$$I_{\alpha\alpha'}(\mathbf{q}) = \int d^2 r_1 \phi^*_\alpha(\mathbf{r}_1) e^{-i\mathbf{q}\cdot\mathbf{r}_1} \phi_{\alpha'}(\mathbf{r}_1), \tag{A21}$$

with the carrier charge $\sigma_\alpha = \sigma_{\alpha'}$ and $\sigma_\beta = \sigma_{\beta'}$. For the coupling of quantum-dot states to continuum states, the Coulomb interaction energy matrix element is

$$W^{\alpha\beta}_{\mathbf{k}\mathbf{k}} = \sum_{\mathbf{q}\neq 0} W_q I_{\alpha\mathbf{k}}(\mathbf{q}) I_{\mathbf{k}\beta}(\mathbf{q}), \tag{A22}$$

where

$$I_{\alpha\mathbf{k}}(\mathbf{q}) = \int d^2 r_1 \phi^*_\alpha(\mathbf{r}_1) e^{-i\mathbf{q}\cdot\mathbf{r}_1} \phi_{\sigma_\alpha\mathbf{k}}(\mathbf{r}_1) \tag{A23}$$

and $\phi_{\sigma\mathbf{k}}(\mathbf{r})$ is the continuum wave function with momentum $\mathbf{k}$ and charge σ. The matrix elements $V^{\alpha\beta}_{\alpha'\beta'}$ and $V^{\alpha\beta}_{\mathbf{k}\mathbf{k}}$ are obtained by replacing the screened Coulomb potential W_q with the bare one V_q in Eqs. (A20) and (A22).

[1] For a text book discussion, see M.O. Scully and M.S. Zubairy, *Quantum Optics* (Cambridge University Press, Cambridge, 1997).
[2] J.P. Marangos, J. Mod. Opt. **45**, 471 (1998).
[3] J. Mompart and R. Corbalan, J. Opt. B: Quantum Semiclassical Opt. **2**, R7 (2000).
[4] S.E. Harris, J.E. Field, and A. Imamoglu, Phys. Rev. Lett. **64**, 1107 (1990).
[5] E.S. Fry, X. Li, D. Nikonov, G.G. Padmabandu, M.O. Scully, A.V. Smith, F.K. Tittel, C. Wang, S.R. Wilkinson, and S.-Y. Zhu, Phys. Rev. Lett. **70**, 3235 (1993).
[6] D.F. Phillips, A. Fleischhauer, A. Mair, R.L. Walsworth, and M.D. Lukin, Phys. Rev. Lett. **86**, 783 (2001).
[7] A.V. Turukhin, V.S. Sudarshanam, M.S. Shahriar, J.A. Musser, B.S. Ham, and P.R. Hemmer, Phys. Rev. Lett. **88**, 023602 (2001).
[8] M. Lindberg and R. Binder, Phys. Rev. Lett. **75**, 1403 (1995).
[9] M.E. Donovan, A. Schülzgen, J. Lee, P.A. Blanche, N. Peyghambarian, G. Khitrova, H.M. Gibbs, I. Rumyantsev, N.H. Kwong, R. Takayama, Z.S. Yang, and R. Binder, Phys. Rev. Lett. **87**, 237402 (2001).
[10] M. Phillips and H. Wang, Phys. Rev. Lett. **89**, 186401 (2002).
[11] M. Phillips and H. Wang, Opt. Lett. **28**, 831 (2003).
[12] A.A. Belyanin, F. Capasso, V.V. Kocharovsky, Vl.V. Kocharovsky, and M.O. Scully, Phys. Rev. A **63**, 053803 (2001).
[13] P.C. Ku, C.J. Chang-Hasnain, and S.L. Chuang, Electron. Lett. **38**, 1581 (2002).
[14] P. Borri, W. Langbein, S. Schneider, U. Woggon, R.L. Sellin, D. Ouyang, and D. Bimberg, Phys. Rev. Lett. **87**, 157401 (2001).
[15] P. Borri, S. Schneider, W. Langbein, U. Woggon, A.E. Zhukov, V.M. Ustinov, N.N. Ledentsov, Z.I. Alferov, D. Ouyang, and D. Bimberg, Appl. Phys. Lett. **79**, 2633 (2001).
[16] H.C. Schneider, W.W. Chow, and S.W. Koch, Phys. Rev. B **64**, 115315 (2001).
[17] M. Lindberg and S.W. Koch, Phys. Rev. B **38**, 3342 (1988).
[18] *GaN and Related Materials*, edited by S.J. Pearton (Gordon and Breach, Amsterdam, 1997), Vol. 2.
[19] M. Fleischhauer, T. McIllrath, and M.O. Scully, Appl. Phys. B: Lasers Opt. **B60**, S123 (1995).
[20] J. Mompart and R. Corbalan, Opt. Commun. **156**, 133 (1998).
[21] V.V. Kozlov, P.G. Polynkin, and M.O. Scully, Phys. Rev. A **59**, 3060 (1999).
[22] V.R. Blok and G.M. Krochik, Phys. Rev. A **44**, 2036 (1991).
[23] Y. Zhu, Phys. Rev. A **53**, 2742 (1996).
[24] W.W. Chow and S.W. Koch, *Semiconductor-Laser Fundamentals: Physics of the Gain Materials* (Springer, Berlin, 1999).
[25] W.W. Chow and H.C. Schneider, Appl. Phys. Lett. **81**, 2566 (2002).
[26] G. Bastard, *Wave Mechanics Applied to Semiconductor Heterostructures* (Les Editions de Physique, Paris, 1988).
[27] *Landolt-Börnstein*, edited by O. Madelung, New Series, Group III (Springer, Berlin, 1987), Vol. 22, Pt. a.